

INVITED PAPER

Monthly Deforestation Monitoring with Sentinel-1 Multi-temporal Signatures and InSAR Coherences

Pulella, A. , Sica, F. , Rizzoli, P. 

Microwaves and Radar Institute, German Aerospace Center (DLR), Münchener Straße 20, 82234 Weßling, Germany.

Abstract: Sentinel-1 interferometric time-series allow for the accurate retrieval of the target's temporal decorrelation and, therefore, the inversion of land cover information and its temporal monitoring. This paper describes the development of an observation scenario for monitoring monthly deforestation over the Amazon rainforest, which relies on the use of radar for overcoming the physical limitations of optical sensors caused by the presence of cloud coverage. Specifically, we implement a classification scheme that exploits multi-temporal SAR features, such as backscatter, spatial textures, and interferometric parameters, to map forested areas. Distinct forest maps are generated for consecutive months and further processed to detect deforestation phenomena and map clear-cuts evolution. The obtained results are validated by selecting cloud-free Sentinel-2 multispectral data on the selected area and acquired during the same observation time.

Key words: forest mapping, deforestation, change detection, Synthetic Aperture Radar, interferometry, interferometric coherence, temporal decorrelation, Sentinel-1, Sentinel-2.

Seguimiento de la deforestación mensual mediante firmas multitemporales Sentinel-1 y coherencias InSAR

Resumen: Las series temporales interferométricas Sentinel-1 permiten la estimación precisa de la decorrelación temporal de la muestra y, por tanto, la recuperación de información acerca de la cobertura terrestre y su seguimiento temporal. Este artículo describe el desarrollo de un escenario de observación para el seguimiento de la deforestación mensual sobre la selva amazónica, basándose en el uso de datos radar para superar las limitaciones físicas propias de los sensores ópticos debido a la presencia de cobertura nubosa. En particular, se ha implementado un esquema de clasificación que explota las características multitemporales SAR, como la retrodispersión, texturas espaciales y parámetros interferométricos, para identificar áreas de bosque. Distintos mapas de bosque para meses consecutivos fueron generados y procesados para detectar fenómenos de deforestación y su evolución. Los resultados obtenidos fueron validados a partir de imágenes Sentinel-2 libres de nubes adquiridas sobre la misma zona y hora de observación.

Palabras clave: cartografía de bosques, deforestación, detección de cambios, Radar de Apertura Sintética, interferometría, coherencia interferométrica, decorrelación temporal, Sentinel-1, Sentinel-2.

To cite this article: Pulella, A., Sica, F., Rizzoli, P. 2020. Monthly Deforestation Monitoring with Sentinel-1 Multi-temporal Signatures and InSAR Coherences. *Revista de Teledetección*, 56, 1-22. <https://doi.org/10.4995/raet.2020.14308>

* Corresponding author: Andrea.Pulella@dlr.de

1. Introduction

The monitoring of forests to maintain a healthy planet is a fundamental aspect of natural resource management. Indeed, forests are the largest carbon reservoirs and are primarily responsible for the presence of oxygen in the atmosphere. They contain up to 80 percent of the aboveground biomass carbon and more than 30 percent of the world's belowground carbon (Ellatifi, 2009). Until the beginning of the 19th century, there had always been a consistent balance between the amount of carbon in forests and in the atmosphere. Unfortunately, since the advent of the industrial era, due to a radical increase in deforestation activities and industrial development, such an equilibrium has been disrupted. The concentration of carbon dioxide (CO_2) in the atmosphere has been steadily increasing ever since, at a rate of about 4 percent per decade (Ellatifi, 2009). In this scenario, a significant role is played by deforestation activities that take place in the Brazilian rainforests (Malhi et al., 2008) and in the Russian boreal forests (Shvidenko & Schepaschenko, 2013).

The development of effective strategies for mapping and monitoring deforestation phenomena is, therefore, of paramount importance to better assess and preserve forest resources worldwide. Among the current analysis instruments, spaceborne remote sensing systems provide an up-and-coming solution for monitoring forest coverage on a global scale, without the need for in-situ measurements (Bontemps et al., 2009; Friedl et al., 2010). Optical sensors, as well as Synthetic Aperture Radar (SAR) are widely used for mapping forest coverage and structure (Dubayah & Drake, 2000; Hansen et al., 2013; Mora et al., 2014; Dobson, 1995; Malenovský et al., 2012). In particular, the latter, providing a day-and-night all-weather conditions imaging capability of the Earth's surface, represents a unique solution for continuous monitoring of large vegetated areas. Indeed, innovative global forest maps have been generated using radar sensors, such as the forest/non-forest map derived from the SAR backscatter of the L-band ALOS/PALSAR system (Shimada et al., 2014) and the global forest/non-forest map extracted from the single-pass volume correlation coefficient estimated from the Interferometric SAR (InSAR) coherence of the X-band bistatic TanDEM-X

system (Martone et al., 2018; Martone et al., 2018; Mazza et al., 2019).

Nowadays, the challenge is to follow deforestation events in nearly real-time aiming, e.g., at providing useful information to the local authorities for a prompt intervention on the ground. A particularly interesting case study is the monitoring of tropical rainforests, broad land areas characterized by a persistent rainy season of more than six months per year, during which trees are hidden continuously under a thick layer of clouds and, therefore, not visible by optical or laser sensors. In this case, radar is mandatory, and last-generation spaceborne sensors are currently delivering an unprecedented quantity of data, which shows extraordinary potential for the development of innovative algorithms. Sentinel-1 is the ESA SAR satellite system, developed within the Copernicus Earth Observation program. It comprises two twin SAR satellites, Sentinel-1A (S-1A) and Sentinel-1B (S-1B), operating at C band in single and dual polarization and flying along the same nominal orbit, shifted by 180 degrees. Sentinel-1 combines wide swath imaging at medium resolution with a significant amount of routine daily acquisitions to form a powerful instrument for forest monitoring with a global reach. Among the four different acquisition modes, in this work, we considered the products provided by the system in the Interferometric Wide swath mode (IW), which guarantees a frequent operational interferometric capability (6 days repeat-pass), covering large areas of 250 km swath with 5 m×20 m spatial resolution (Torres et al., 2012). The IW mode has proven to be a potentially powerful acquisition mode for global forest mapping since it is possible to create multi-temporal algorithms able to merge the properties of SAR backscatter and interferometric features (Sica et al., 2019; Pulella et al., 2020).

In this paper, we now demonstrate such capabilities through a specific analysis about detecting changes in the Amazon rainforest, by exploiting the processing chain presented in Pulella et al. (2020). In particular, we consider interferometric short-time-series, i.e., five S-1A/B acquisitions corresponding to about one month of observations, acquired over the Rondonia state, Brazil. We select as test site an area located between the state of Rondonia, the state of Acre, and the state of Amazonas, along a curve that hugs the southeastern edge of the forest, commonly called

the *arc of deforestation* (Diniz et al., 2013). We consider three consecutive months of Sentinel-1 acquisitions over this area to follow the evolution in time of detected clear-cuts.

The paper is structured as follows. Section 2 illustrates the data sets used in this work: the Sentinel-1 short-time-series acquired over the state of Rondonia, the external references used for the training and validation of the classification algorithm, and finally, the Sentinel-2 optical data used for a first validation of the monthly deforestation detected using Sentinel-1. Section 3 recalls the proposed method, based on the combined exploitation of the textural information retrieved from the backscatter and the interferometric coherence derived from S-1 interferometric short-time-series. The retrieved parameters are subsequently used as input features to a Random Forests classifier to generate forest maps. Forest loss is then evaluated by comparing two consecutive forest maps. The obtained results regarding both forest classification and forest loss detection are collected and discussed in Section 4. Finally, Section 5 summarizes the findings and presents a brief outlook on possible future developments of the proposed methodology.

2. Materials

In this section we describe the test site location, the Sentinel-1 data set and the reference data considered in this work.

2.1. Test area: southern Brazilian Amazon

The results presented in this work concern a large region of about 44 million hectares highlighted in red in Figure 1 and located in the southern Brazilian

Amazon, comprising the state of Rondonia, the eastern side of the state of Acre, and a small area close to Boca do Acre, a municipality in the state of Amazonas. This region is of general interest since it is part of the Amazonian *arc of deforestation*, a belt of rapidly disappearing tropical forest that follows the southern margin of the Amazon and bends northeastward toward the bank of the Amazon River mouth. In particular, we can distinguish a portion of the Amazonia biome in our test site surrounding the broad area of plantations in Rondonia. The biome consists of five vegetation types (Perigolo et al., 2017):

- Open ombrophilous forest, here the most frequently encountered one.
- Dense ombrophilous forest.
- Alluvial ombrophilous forests.
- Semideciduous forests.
- Campinaranas, i.e., stunted vegetation dominated by small trees with thin stems.

On the contrary, this specific plantation area is mainly used for soybean production for about 40 years. Indeed, Rondonia is the first Brazilian state where forest logging and clearing began with road expansion in the 1970s and 1980s, supported by the government, which introduced farming and mining operations (Stone et al., 1991). In the last decades, industrial-scale agriculture, particularly cattle ranching and soybean farming, has become an increasingly important cause of deforestation in the area. Since the *arc of deforestation* is expanding north towards the heart of the Amazon basin, an analysis of the activities at the borders of this region is of extreme importance.

2.2. Sentinel-1 data

In order to monitor the state of the rainforest in the southern Amazon, the European Space Agency (ESA) planned, between the end of April 2019 and the end of December 2019, a denser SAR coverage using Sentinel-1A and Sentinel-1B satellites over such an area, reaching a constant repeat cycle of 6 days.

Accordingly, we downloaded a set of S-1 IW short-time-series over 12 adjacent footprints and we processed each of them following the framework presented in Subsection 3.1. Figure 2 depicts



Figure 1. Google Earth image over the Amazon basin with in red the test site location.

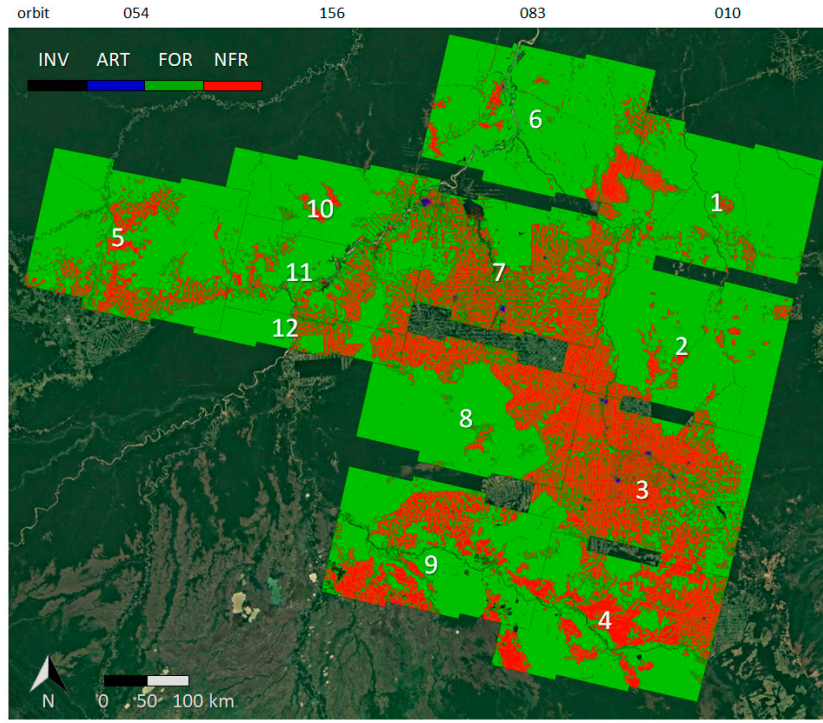


Figure 2. Finer Resolution Observation and Monitoring of Global Land Cover (FROM-GLC, 2017) reference map chosen for the training and validation stages. Black: *invalid pixels* (INV), blue: *artificial surfaces* (ART), green: *forests* (FOR), red: *non-forested areas* (NFR). The white numbers identify the corresponding Sentinel-1 IW footprints, described in Table 1, while the numbers at the top show the orbits associated to the different acquisitions.

the 12 S-1 footprints (identified with a white number) and, for each of them, shows the FROM-GLC external reference map that we used for training and testing the algorithm, described in detail later on in Subsection 2.3.

In particular, the Random Forests model described in Section 3 was created by considering random samples extracted from 11 S-1 short-time-series associated to distinct footprints, by considering as observation time the month of May 2019. The

Table 1. Sentinel-1 footprints description. From left to right: stack number, relative orbit number, name of the time-series associated to the orbit number, corner coordinates in latitude (Lat. Min and Lat. Max) and longitude (Lon. Min and Lon. Max). Footprint number 5, marked with an asterisk, is chosen for the validation and the change detection stages, while all the others are used for training the Random Forests algorithm.

Sentinel-1 Corner Coordinates [deg]						
Footprint	Orbit	Name	Lat. Min	Lat. Max	Lon. Min	Lon. Max
1	010	TS_0	9°40'58.34"S	7°42'53.99"S	59°52'18.71"W	61°44'43.20"W
2	010	TS_1	11°16'36.74"S	9°15'31.41"S	60°12'59.94"W	62°5'1.52"W
3	010	TS_2	12°45'21.09"S	10°43'21.81"S	60°33'23.20"W	62°26'23.22"W
4	010	TS_3	14°10'32.67"S	12°12'43.74"S	60°53'48.14"W	62°46'54.92"W
5*	054	TS_0	10°12'15.96"S	8°4'40.60"S	66°8'34.73"W	67°59'40.25"W
6	083	TS_0	8°51'9.51"S	6°50'56.20"S	61°42'32.10"W	63°36'0.35"W
7	083	TS_1	10°22'8.36"S	8°32'54.94"S	62°4'44.36"W	63°37'30.02"W
8	083	TS_2	11°51'16.77"S	10°2'26.15"S	62°25'15.09"W	64°19'5.05"W
9	083	TS_3	13°24'3.87"S	11°32'42.18"S	62°44'38.52"W	64°40'34.71"W
10	156	TS_0	9°24'34.67"S	8°4'15.76"S	63°53'30.37"W	65°56'1.88"W
11	156	TS_1	10°15'7.76"S	8°48'35.78"S	64°5'7.05"W	66°8'22.17"W
12	156	TS_2	10°36'21.14"S	9°46'22.31"S	64°9'39.68"W	66°19'6.56"W

coordinates of the associated footprints used for the training of the RF algorithm are reported in Table 1. Footprint number 5, marked with an asterisk, is not included in the training stage. Since the region that it covers corresponds to an area on the edge of the *arc of deforestation*, we selected it as a test set for monitoring on-going deforestation phenomena.

Therefore, we downloaded 3 S-1 short-time-series over footprint number 5, acquired in three consecutive months: May, June, and July 2019, respectively. Figure 3 encapsulates in a calendar the acquisition dates of the complete dataset of Sentinel-1 data considered in this work. The square and circular markers identify which sensor, between S-1A and S-1B, acquires on a specific date. Each relative orbit number within a certain month is highlighted with a different color and contains a different number of footprints on which one can extract short-time-series, named as *TS*. Furthermore, the footprints associated with a relative orbit number and analyzed on a precise observation time have in common the same

reference acquisition (master image) for performing the multi-temporal coregistration.

2.3. External reference data

In this subsection, we detail the independent data sets used for both training and testing the proposed methodology.

According to (Pulella et al., 2020), we trained and validated the monthly forest maps from S-1 on a modified version of the Finer Resolution Observation and Monitoring of Global Land Cover (FROM-GLC) map (Gong et al., 2019). It consists of a high-resolution (10 m) inventory of land cover in 10 classes at a global-scale, generated by exploiting Sentinel-2 data acquired over the year 2017. The strategy adopted for the generation of the version of the FROM-GLC in 4 classes shown in Figure 2 is reported in Subsection 3.2.

Furthermore, in order to take into account all the possible temporal inconsistencies between FROM-GLC reference and Sentinel-1, we considered as additional reference the PRODES

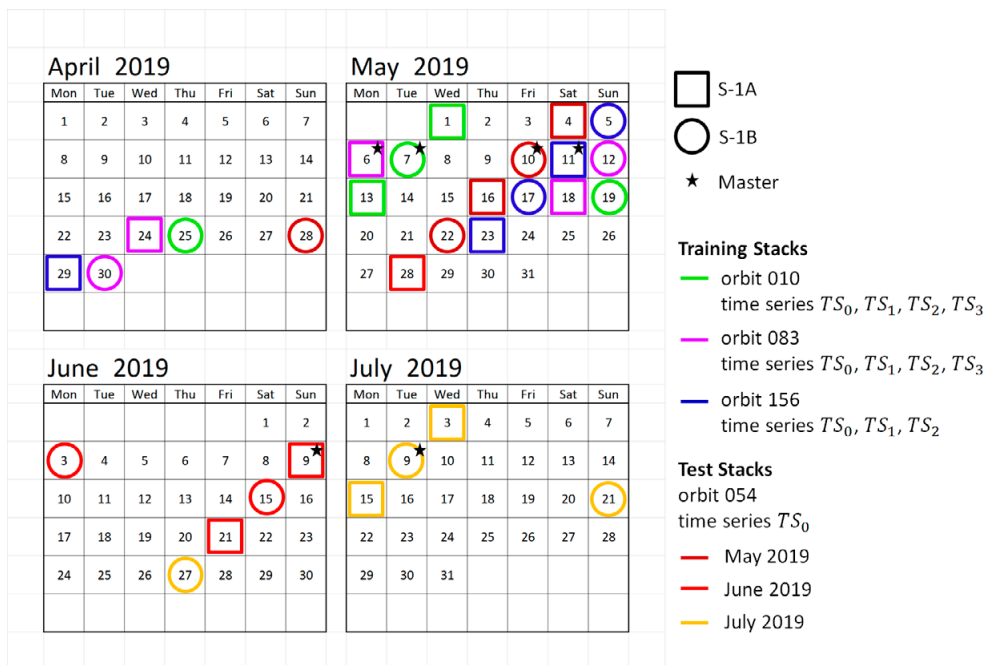


Figure 3. Sentinel-1 acquisition dates description. A star represents the master image, while the dates marked with squares (S-1A) and circles (S-1B) represent the slave images. In general, each relative orbit has a different number of footprints associated with different time series. A different color is associated with those time series acquired within a certain month and related to the same relative orbit number.

(*Programa de Cálculo do Desflorestamento da Amazônia*) digital map (Valeriano et al., 2004). PRODES consists of a ground polygon inventory, steadily updated (every year, officially on the 1st of August) to the new deforestation areas on the whole Amazon rainforest. Although PRODES is a medium-resolution (30 m) product derived from visual inspection of optical data and does not identify patches of loss smaller than 6.25 ha (Kalamandeen et al., 2018), we extracted from it the polygons corresponding to new cuts occurred between 2017 and 2019, indicated in the paper as PRODES 2018 and PRODES 2019, respectively. We used both the set of polygons for two different purposes:

- classification performance evaluation of the monthly forest maps: we set both of the PRODES deforestation polygons as invalid samples in the modified FROM-GLC map, obtaining a more reliable map that discards all the changes occurred between 2017 and 2019.
- monthly clear-cuts detection: we used the clearing areas detected by PRODES in 2018 and 2019 separately for visual comparison with the results of S-1 monthly change detection.

Finally, we used the S-2 data just for validating the monthly results of the proposed algorithm over small selected areas comprised within the test acquisition location.

3. Methodology

In this paper, we detect deforestation monthly by exploiting the Sentinel-1 interferometric time series. The presented algorithm is a follow-up of the methodology in (Sica et al., 2019). Temporal decorrelation can indeed be considered a characteristic of the imaged target and therefore brings useful information about the land cover (Sica et al., 2004). We compute temporal decorrelation at the C-band from the Sentinel-1 constellation and use it to map forested areas at medium resolution and accuracy (Pulella et al., 2020). This section is organized into three subsections, addressing the different approaches carried out during the analysis. Subsection 3.1 recalls the principal aspects of the latest version of the algorithm based on Sentinel-1 short-time-series, proposed in (Pulella et al., 2020). Subsection 3.2 illustrates the strategy adopted for aggregating the classes in the

FROM-GLC digital map. Subsection 3.3 describes the approach adopted for detecting the monthly changes in the forest and, finally, Subsection 3.4 presents the flowchart used for selecting and pre-processing Sentinel-2 tiles for the validation of the obtained results.

3.1. Sentinel-1 short-time-series for Forest Mapping

The processing chain presented in Sica et al.(2019) and enhanced in Pulella et al. (2020), is recalled here in Figure 4. Starting from a set of five focused S-1 Interferometric Wide- Swath (IW) acquisitions in VV polarization, which corresponds to a monthly observation time, the chain performs a coregistration of the entire stack to the reference master image, selected as the one in the middle of the considered temporal interval. Subsequently, the backscatter and its spatial textures and the interferometric parameters are computed following two different branches.

In particular, we proposed in Pulella et al. (2020) the exploitation of the texture information contained in the backscatter by applying the Sum And Difference Histograms (SADH) methodology (Unser, 1986). This method allows for the definition of a set of spatial textures using two probability distributions, respectively retrieved by measuring the local sum and the local difference between the starting image and its shift along a spatial direction.

Overall, we utilize the following features with a spatial resolution of 50 meters:

- the multi-temporal backscatter coefficient γ^0 , estimated as the average γ^0 along the temporal direction,
- two set of SADH textures, $SADH_{(1,0)}$ and $SADH_{(0,1)}$, each one obtained by considering a different but significant displacement vector along the azimuth $d=(1,0)$ and the slant-range $d=(0,1)$ directions, respectively,
- the interferometric parameters τ and ρLT , respectively called *temporal decorrelation constant* and *long-term coherence*, both estimated from a two parameters exponential fitting model describing the temporal decorrelation contribution of a single target.

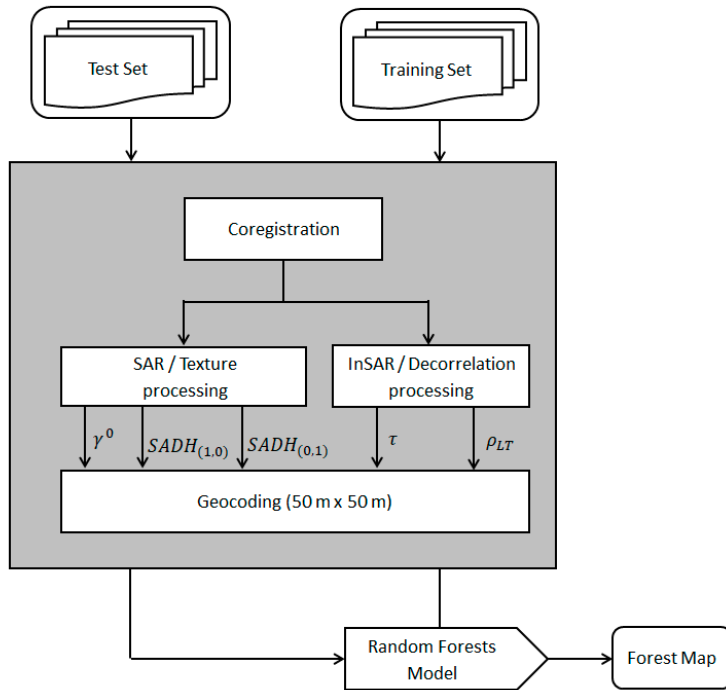


Figure 4. Sentinel-1 processing chain for short-time-series, based on the architecture presented in Sica et al. (2019), with the integration of Sum and Difference Histograms (SADH) textures proposed in Pulella et al. (2020).

All of them are then used as input to the machine learning Random Forests (RF) classifier (Breiman, 2001). This supervised learning algorithm has already been widely exploited at the aim of land cover classification (Belgiu & Drăguț, 2016). As depicted in Figure 4, the first necessary step to apply this classifier is the proper training of the model, starting from a training data set that is independent of the data set used for testing. To do so, we select as inputs all features retrieved from the backscatter and interferometric coherence within the short-time-series and the Finer Resolution Observation and Monitoring of Global Land Cover (FROM-GLC) map (Gong et al., 2019) as an external reference. Therefore, the algorithm randomly selects from the training set a large number of pixels for each class. It replicates the pixels belonging to those classes with low data availability to respect the balance among classes. In particular, according to Pulella et al. (2020), we select 5 million pixels for each of the three classes proposed in (Sica et al., 2019), i.e., artificial surfaces (ART), forests (FOR), and non-forested areas (NFR), and

we replicate the samples of the class ART for reaching a well-balanced training data set. The Random Forests then creates one decision tree at a time using the following iterations: (1) it computes the node of a decision tree by setting the feature's subset size as the square root of the total number of features and using the Gini Impurity as the best split method. Hence, (2) the algorithm repeats the previous step until a certain number of nodes have been reached; in our case, we chose as metric the minimum number of samples required to be at a leaf node, and we fixed it to 50. Finally, (3) the complete RF model, i.e., the overall set of trees, is built-up by repeating all steps N times to create N trees; in this work, we use 50 decision trees as in Pulella et al. (2020). After the Random Forests decision trees and classifiers are created, predictions can be made on each sample of the test set by (1) run the test features through the rules of each decision tree to predict the outcome, (2) calculate the votes for each predicted target and (3) choose the most voted estimated target as the final prediction.

3.2. FROM-GLC: classes aggregation and updating to Sentinel-1 data

In order to use a more recent and reliable reference, comparable with the forest maps of 2019, we performed classes aggregation on the FROM-GLC map of 2017, followed by a pixel masking over those areas where changes occurred between 2017 and 2019. In particular, we first grouped the classes of the FROM-GLC map into four macro-classes: artificial surfaces (ART), forests (FOR), non-forested areas (NFR), and water bodies and unclassified or no data as invalids (INV), following the strategy described in Table 2.

Secondly, we removed from the reference all the deforestation samples detected by PRODES 2018 and 2019. As a results, we obtained a trustworthy digital map for training the Random Forests algorithm and, therefore, for a consistent performance evaluation of both the three consecutive S-1 forest maps.

Table 2. Finer Resolution Observation and Monitoring of Global Land Cover (FROM-GLC) classes aggregation strategy: artificial surfaces (ART), forests (FOR), non-forested areas (NFR), and water bodies and unclassified or no data as invalids (INV).

FROM-GLC	Higher-Level Class
Unclassified	
Water	INV
Snow/Ice	
Impervious surface	ART
Forest	FOR
Cropland	
Grassland	
Shrubland	
Wetland	NFR
Tundra	
Bareland	

According to Pulella et al. (2020), the performance analysis is carried out through the computation of the overall accuracy (OA) and average accuracy (AA), respectively defined in a binary problem as:

$$OA = \frac{TP + TN}{TP + TN + FP + FN} \quad (1)$$

and

$$AA = \frac{1}{2} \left(\frac{TP}{TP + FN} + \frac{TN}{TN + FP} \right) \quad (2)$$

where TP , TN , FP , and FN denote, respectively, the number of true positives, true negatives, false positives, and false negatives. We measured both the metrics on all the valid pixels of the modified version of the FROM-GLC reference map. In particular, the average accuracy, also called mean producer's accuracy, defines the sum of accuracies per class divided by the total number of classes, while the overall accuracy corresponds to the total number of correctly classified pixels divided by the total number of test pixels. These two metrics are complementary. Indeed, the overall accuracy quantifies the global performance of the classifier, while the average accuracy measures the accuracy balance among the different classes.

3.3. Monthly Change Detection

Change detection may be applied at a variety of different conceptual levels. The simplest form would be to differentiate between subsequent pixel values in time (Bueso-Bello et al., 2018), whilst the most complex might be between high-level descriptions such as towns, forests, etc. (Wen et al., 2016; Lu et al., 2017). The kind of change detection that we consider here lies in between these two extremes. It is a change detection between small objects detected by simple segmentation.

The algorithm is summarized in Figure 5. Since we expect that changes will happen on adjacent pixels, we aim to detect a whole area by performing pixel clustering. We apply an image segmentation based on morphological watershed transformation (Beucher & Meyer, 1993) that regards the image

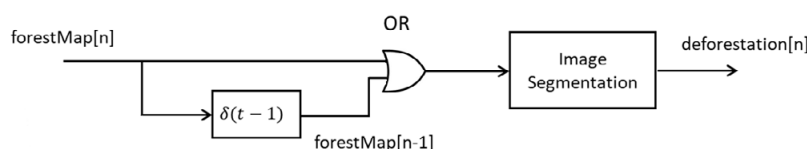


Figure 5. Scheme of the automatic system for evaluating the deforestation on the n -th month. The block $\delta(t - 1)$ represents the 1-month delay that has to be considered for getting the deforestation map.

intensity as a topographic map and is very useful to this purpose. The use of a segmentation algorithm to identify the clear-cuts polygons has two main advantages. It first identifies groups of pixels that are likely to be associated with the same physical object on the ground. Moreover, this also allows for a certain tolerance with respect to remaining image misalignments, which might arise from small residual image distortions. Secondly, segmentation offers an adaptive smoothing of the image pixel values depending on region size. Using the watershed algorithm we can guarantee the detection of clear-cuts not smaller than 75 ha.

3.4. Sentinel-2 for monthly validation

Sentinel-2 images are used as an external reference for the validation of the monthly forest/non-forest classification over specific regions of interest. In particular, we consider two aspects of the vegetation, which can be translated into vegetation indexes derived from multispectral data: plant health and water stress. Indeed, vegetation absorbs solar radiation in different bands and emits back a different percentage of it. The percentage of reflected radiation in specific bands, such as near-infrared (NIR), red (RED), and short-wave infrared (SWIR), concurs to the definition of the following two different vegetation indices: (1) the NDVI, i.e. the Normalized Difference Vegetation Index, and (2) the NDMI, which stands for Normalized Difference Moisture Index. The former describes the vigor level of a vegetated area and it is calculated as the ratio between the difference and the sum of the reflected radiations in the near-infrared and in the red channels:

$$NDVI = \frac{NIR - RED}{NIR + RED} = \frac{B08 - B04}{B08 + B04} \quad (3)$$

where NIR stands for near-infrared band and falls roughly between 760 and 900 nanometers, and RED is the visible red channel from 650 to 680 nanometers, corresponding using Sentinel-2 to band 8 (B08) and band 4 (B04), respectively (Drusch et al., 2012). The NDVI varies between -1 and 1. Considering that the rainforest may be explained as an area with high canopy cover and high vigor, we decided to create a forest/non-forest map by setting as forest all those pixels with NDVI higher than 0.7.

Differently, the NDMI is an informative index, used to determine vegetation water content (Wilson & Sader, 2002). It is calculated as the ratio between the difference and the sum of the reflected radiations in the near-infrared and short-wave infrared bands:

$$NDMI = \frac{NIR - SWIR}{NIR + SWIR} = \frac{B08 - B11}{B08 + B11} \quad (4)$$

where NIR is the above mentioned near-infrared channel, while SWIR is the Short-Wave Infrared band, which typically ranges from 1550 to 1750 nanometers. Although the NDMI was originally developed for use with Landsat Thematic Mapper (TM) bands 4 (NIR) and 5 (SWIR) (Wilson & Sader, 2002), we replicate it using Sentinel-2 bands 8 (B08) and 11 (B11) (Drusch et al., 2012). In this work, the NDMI is used together with the RGB image just for a visual evaluation of the results. Furthermore, because of the strong dependency of Sentinel-2 data on clouds and cloud shadows, we generate an additional mask, that we call *Unclassified mask*, useful for the measure of the cloud cover percentage of each acquisition. In particular, this mask is obtained by merging the cloud and the cloud shadow layers inside the Scene Classification (SCL) map, a thematic map freely available in the S-2 Level-2A products (Main-Knorr et al., 2017). Given a set of *Unclassified masks*, we select the mostly cloudless S-2 acquisition, i.e. the optical image whose cloud cover percentage is the minimum one within the S-1 stack observation time. The presented methodology can be schematized as in Figure 6.

During the downloading of the S-2 tiles, a first selection is applied in order to consider only those S-2 acquisitions whose footprint falls within the test site region, previously fixed in the S-1 processing chain of Figure 4. Then a for loop loads in a buffer all the available tiles, merges them using a mosaicking algorithm and finally stores the result, i.e. the strip associated to the acquisition date. The loop continues until the complete span of all S-2 acquisition dates within the S-1 observation time. The result is a stack of Sentinel-2 mosaicked images, covering the S-1 test site. The main benefit of this approach is the possibility to automatically select the most cloudless S-2 acquisition, i.e. the one with the lowest cloud cover percentage, given the coordinates of a smaller region of interest in

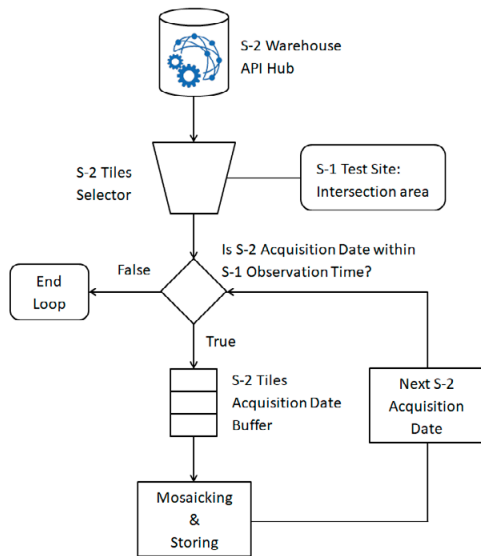


Figure 6. Flow diagram of the automatic system for the generation of S-2 mosaicked images over the S-1 region of interest, which corresponds to the intersection area among the S-1 acquisitions in the short-time-series.

the test site. Figure 7 shows an example of the results generated by the above mentioned automatic system over a dedicated patch. In this specific case, the algorithm estimates a cloud cover percentage of 22.40% over the patch. In Section 4 we will show the NDVI mask and the NDMI map,

with superimposed the missing data (MDA) and unclassified data (UNC) pixels of the *Unclassified mask*. The MDA class comprises two different types of invalid pixels. The former belong to areas out of the S-2 footprint in a precise acquisition date, and the latter is linked to areas within the S-2 footprint where the sensor did not acquire.

By discarding the invalid pixels, we evaluate four metrics: the overall accuracy (OA) considering all the classes, and precision (P), recall (R), and F1-score (F1) for the forest class (FOR). In the latter case, we refer to a binary problem by considering as reference the NDVI mask and the classes *forest* (FOR) and *others* (OTH). On the one hand, the overall accuracy of equation (1) measures the performance of our classification model. On the other hand, the remaining three metrics refer to the model's effectiveness in recognizing a specific class, in our case, the FOR class. Precision (P) and recall (R) are respectively defined as:

$$P = \frac{TP}{TP+FP} \quad (5)$$

and

$$R = \frac{TP}{TP+FN} \quad (6)$$

The precision and recall determine the cost of a false alarm and the classifier's capability to detect

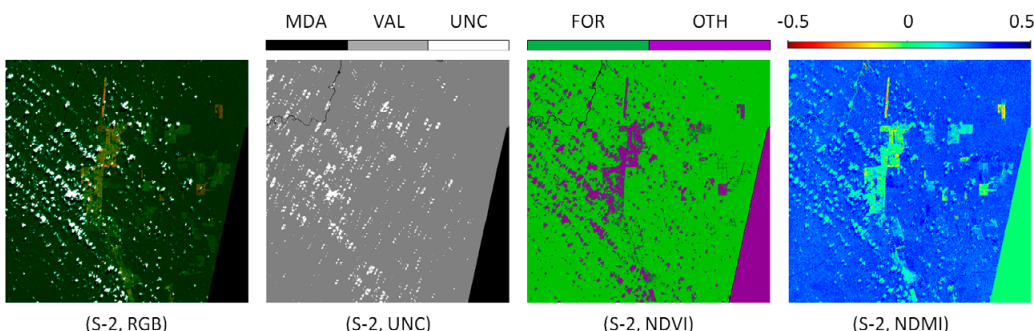


Figure 7. Exemplary results for the pre-processing of S-2 data. From left to right: (S-2, RGB) is the True Color map extracted from the S-2 acquisition of 29.05.2019 over a 1024×1024 patch in the Amazon rainforest; (S-2, UNC) is the *Unclassified mask* where black are missing data pixels (MDA), gray are valid pixels (VAL) and white are the unclassified data (UNC), i.e. clouds (dense and medium cirrus) cloud shadows; (S-2, NDVI) is the NDVI mask obtained by thresholding the associated index at 0.7, obtaining two classes, forests (FOR) and others (OTH) which represents non-vegetated areas and missing data; (S-2, NDMI) is the NDMI index stretched between -0.5 and 0.5 for enhancing the visual representation. Blue: humid areas, Red: dry areas, e.g. clear-cuts, Green: values close to 0, representing medium humidity areas and missing values.

a forest pixel correctly, respectively. The F1-Score, eventually, aggregates the latter two measures to give a summary score and is defined as follows:

$$F1 = \frac{2 \cdot P \cdot R}{P + R} \quad (7)$$

The F1-Score reaches its maximum at 1 when both precision and recall are 1. It can be interpreted as a weighted average of precision and recall and considers both false positives and false negatives.

4. Results and Discussion

In this section, we present and discuss the experimental results obtained by applying the processing framework proposed in Section 3. Out of the 12 footprints described in Figure 2 and Table 1, we select footprint number 5 for testing the RF algorithm and detecting changes monthly, and we process three different short-time-series acquired in three consecutive months over such a region. Differently, we processed the sole short-time-series of May 2019 on the remaining 11 footprints, and we used them for training the RF algorithm.

Figure 8 shows a pie chart representing the feature importance associated with the dedicated training set. All the texture features are grouped in a single variable, named SADH. According to Pulella et al. (2020) we notice that the set of SADH textures plays a relevant role in the Random Forests prediction.

Figure 9 shows the reference map over footprint 5, used for the performance evaluation: we updated the FROM-GLC map of 2017 with the PRODES

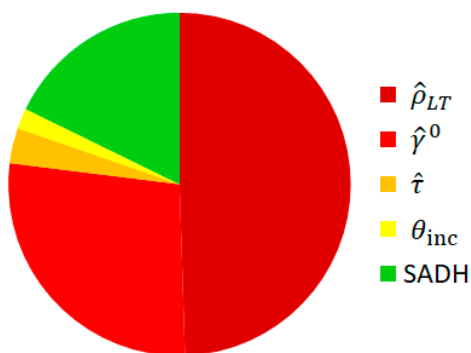


Figure 8. Feature importance for the input parameters used in the Random Forests classifier.

polygons (in white) referring to the deforestation occurred between the 1st of August 2017 and the 31st of July 2019.

Table 3. Overall accuracy (OA) and average accuracy (AA) of the forest maps extracted from the three consecutive months over the footprint number 5 in Table 1 and drawn in Figure 9.

Metric	May 2019	June 2019	July 2019
OA	92.82%	91.04%	88.65%
AA	85.21%	83.7%	83.02%

Table 3 reports the performance of the different S-1 forest maps, extracted from the short-time-series of May 2019, June 2019, and July 2019, respectively. All forest maps exceed an overall agreement (OA) of 88% and, at the same time, guarantee a well-balance in the classification among the three considered classes, with average accuracies (AA) higher than 83%.

The reliability of the derived forest map allows us to apply the change detection chain presented in Figure 5. Accordingly, we first visually compare clear-cuts detected by our algorithm with the polygons provided by PRODES on a large-scale basis. The reader should be aware that the PRODES polygons cover a much larger period than the S-1 short-time-series so that additional incongruencies caused by different observation intervals are expected and unavoidable.

For comparison, Figure 10 shows two FROM-GLC maps in grayscale with superimposed colored polygons identifying clear cuts. The reference map on the left-hand-side depicts the annual deforestation hand-marked by PRODES in 2018 (yellow) and 2019 (red). Together, they correspond to the white polygons in Figure 9. The image on the right-hand-side summarizes our S-1 results obtained by processing three short-time-series in 3 different colored sets of polygons. The polygons in pink correspond to the deforestation period called May 2019: they are detected by comparing the FROM-GLC of 2017 with the forest map estimated using the short-time series of May 2019. The polygons in orange (June 2019) are obtained by comparing the S-1 forest map of May 2019 with the one of June 2019, and finally, the polygons in cyan (July 2019) are the results of the comparison between the S-1 forest map of June 2019 and the one of July 2019.

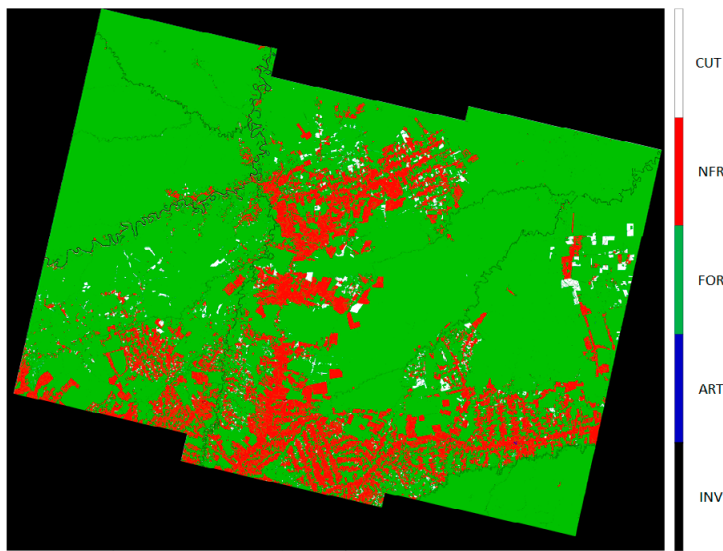


Figure 9. Finer Resolution Observation and Monitoring of Global Land Cover (FROM-GLC, 2017) reference map with in white the clear-cuts (CUT) detected by PRODES between 2017 and 2019. Black: *invalid pixels* (INV), blue: *artificial surfaces* (ART), green: *forests* (FOR), red: *non-forested areas* (NFR), white: *clear-cuts* (CUT).

Figure 10 shows a certain consistency among the polygons detected by our algorithm and the ones identified by PRODES. Nevertheless, two issues have to be considered. The first one relies on the clear-cuts detection of May 2019: there is an almost two years gap between the FROM-GLC

2017 and the first short- time-series of May 2019; during such a long time, we are unable to distinguish if our detected clear-cuts correspond to PRODES polygons detected in 2018 or to the ones identified in 2019. Still, we can observe that some areas hand-marked by the analysts in 2019 may be

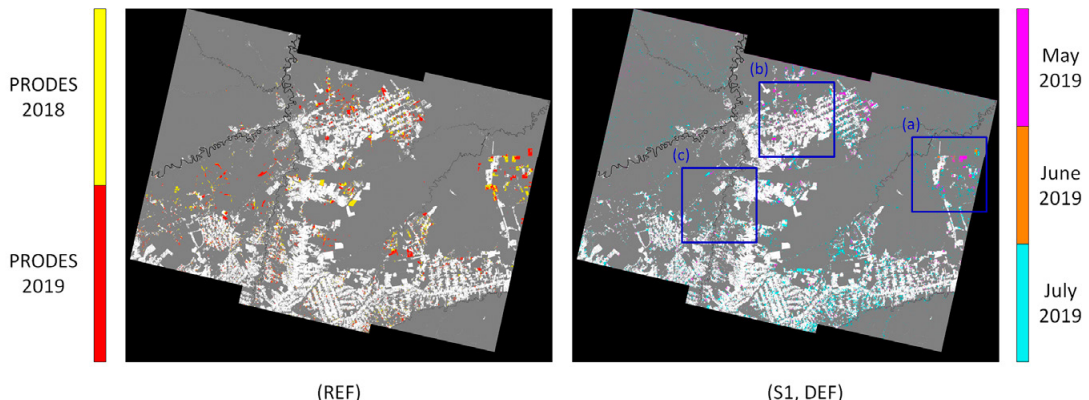


Figure 10. Comparison between the reference map (left), i.e., the annual deforestation marked by PRODES on the 1st of August 2018 (yellow) and on the 1st of August 2019 (red), and our deforestation S-1 map (right) explaining the changes detected in three consecutive time intervals. Pink: clear-cuts between FROM-GLC 2017 and May 2019, Orange: clear-cuts between May and June 2019, Cyan: clear-cuts between June and July 2019. Both the set of polygons are superimposed to the FROM-GLC 2017 of Figure 9, here represented in grayscale for the sake of clarity. Blue polygons identify three patches of 1024×1024 pixels used for the classification accuracy analysis. They are named (a), (b), and (c).

addressed as cleared (1) before June 2019, (2) in June 2019, or (3) in July 2019. The second issue refers to the reliability of the polygons provided by PRODES. Indeed, this ground inventory does not identify forest loss patches smaller than 6.25 ha even though the nominal resolution is 30 m (Kalamandeen et al., 2018; Montibeller et al.,

2020). This criterion results in a lower error at the cost of limiting the detection of smaller patches.

Within the selected test area of footprint 5, we now concentrate on the analysis of three different patches of 1024×1024 pixels size, indicated as (a), (b), (c), and highlighted in blue in Figure 10. In

Table 4. Sentinel-2 acquisitions over the selected S-1 test area. The table is divided into three rows, each one addressing the month defined for S-1 short-time-series: May 2019, June 2019, and July 2019. From left to right: S-1 month, S-1 starting and ending dates of the short-time-series, S-2 acquisition date, S-2 sensor name, and cloud cover percentage (%) of the patch (a), patch (b), patch (c).

Sentinel-2 Cloud Cover Percentage [%]							
S-1 Month	S-1 Start	S-1 End	S-2 Date	S-2 Sensor	Patch (a)	Patch (b)	Patch (c)
May 2019	2019.04.28	2019.05.22	2019.04.27	S-2B	no-data	0.04*	2.18
			2019.04.29	S-2A	47.35	no-data	no-data
			2019.05.02	S-2A	no-data	14.30	14.50
			2019.05.04	S-2B	100	no-data	no-data
			2019.05.07	S-2B	no-data	5.79	1.39
			2019.05.09	S-2A	0.18*	no-data	no-data
			2019.05.12	S-2A	no-data	89.68	98.05
			2019.05.14	S-2B	94.65	no-data	no-data
			2019.05.17	S-2B	no-data	1.07	0.05*
			2019.05.19	S-2A	77.97	no-data	no-data
June 2019	2019.05.29	2019.06.21	2019.05.22	S-2A	no-data	29.15	4.74
			2019.05.29	S-2A	22.40	no-data	no-data
			2019.06.01	S-2A	no-data	31.35	92.06
			2019.06.03	S-2B	94.29	no-data	no-data
			2019.06.06	S-2B	no-data	1.10*	1.33
			2019.06.08	S-2A	60.29	no-data	no-data
			2019.06.11	S-2A	no-data	7.14	1.02*
			2019.06.13	S-2B	41.94	no-data	no-data
			2019.06.16	S-2B	no-data	4.04	1.23
			2019.06.18	S-2A	0.02*	no-data	no-data
July 2019	2019.06.28	2019.07.21	2019.06.21	S-2A	no-data	2.12	6.77
			2019.06.28	S-2A	17.54	no-data	no-data
			2019.07.01	S-2A	no-data	0.02*	1.21
			2019.07.03	S-2B	9.44	no-data	no-data
			2019.07.06	S-2B	no-data	100	99.99
			2019.07.08	S-2A	0.01*	no-data	no-data
			2019.07.11	S-2A	no-data	1.66	0.04*
			2019.07.13	S-2B	70.22	no-data	no-data
			2019.07.16	S-2B	no-data	22.89	9.50
			2019.07.18	S-2A	1.09	no-data	no-data

this case, the analysis is carried out by comparing the monthly S-1 forest map with three vegetation parameters derived from S-2 acquisitions: the NDVI mask, the NDMI map, and the RGB map, all masked with the invalid pixels of the *Unclassified mask*, as presented in Subsection 3.4.

We exploited the *Unclassified mask* to evaluate the cloud cover percentage of all available acquisitions over the different patches. In particular, Table 4 reports the cloud cover percentage for patch (a), patch (b), and patch (c) on all the S-2 acquisitions from May 2019, June 2019, and July 2019, respectively. Since the flow diagram depicted in Figure 6 is an automatized procedure, we can see that in both months, some mosaicked images do not cover the considered patches. Those cases are marked as no-data. On the contrary, when comparing the values of cloud cover percentage, we can appreciate that for each month and each patch, we have a different sufficiently reliable

S-2 acquisition. Furthermore, we observe that, although we consider three months during the dry season, we can extract for each patch no more than one cloud-free acquisition per month with respect to the five/six ones available. In Table 4, we mark with asterisks the most reliable acquisition for each patch during each month, used for validating the experimental results.

The comparison between the S-1 forest maps and the S-2 vegetation parameters for patches (a), (b), and (c) are reported in detail in Figure 11, Figure 12, and Figure 13, respectively.

Figure 11 shows an area where activities were on-going in Summer 2019. Besides the missing data on the S-2 acquisition of June 2019, we can identify at least two deforestation hot spots, indicated as (i) and (ii) and delimited by yellow circles in Figure 11, over which deforestation started from June 2019. Furthermore, by comparing the

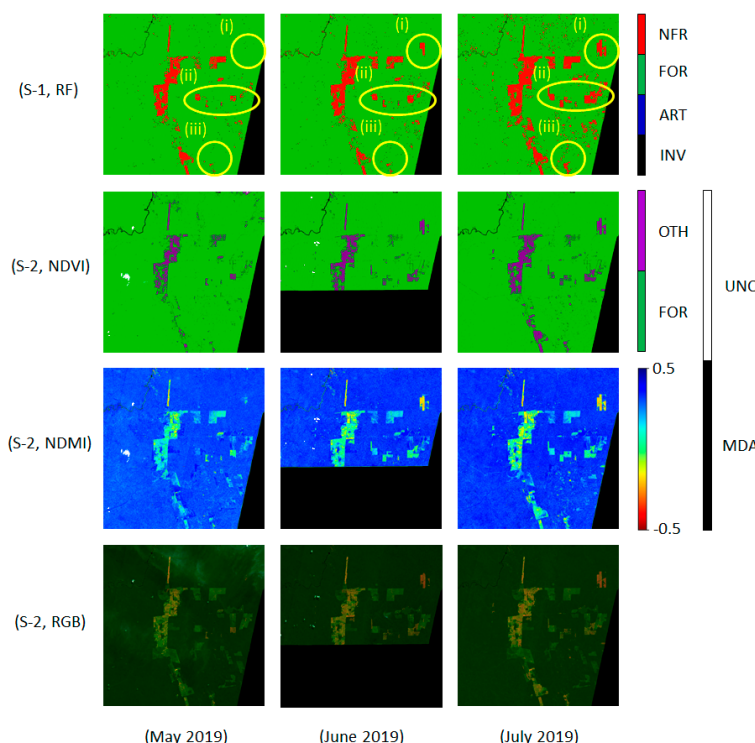


Figure 11. Patch (a): monthly classification comparison between S-1 forest map and S-2 parameters. The columns indicate the three consecutive months on which we selected the S-1 short-time-series and the S-2 mostly cloudless acquisition; the rows indicate the analyzed outcomes: the forest map generated using the RF classifier on the S-1 stack (S-1, RF), and the NDVI mask, NDMI, and RGB maps retrieved from S-2. The yellow circles in (S-1, RF) identify three separated hot spots, named (i), (ii) and (iii).

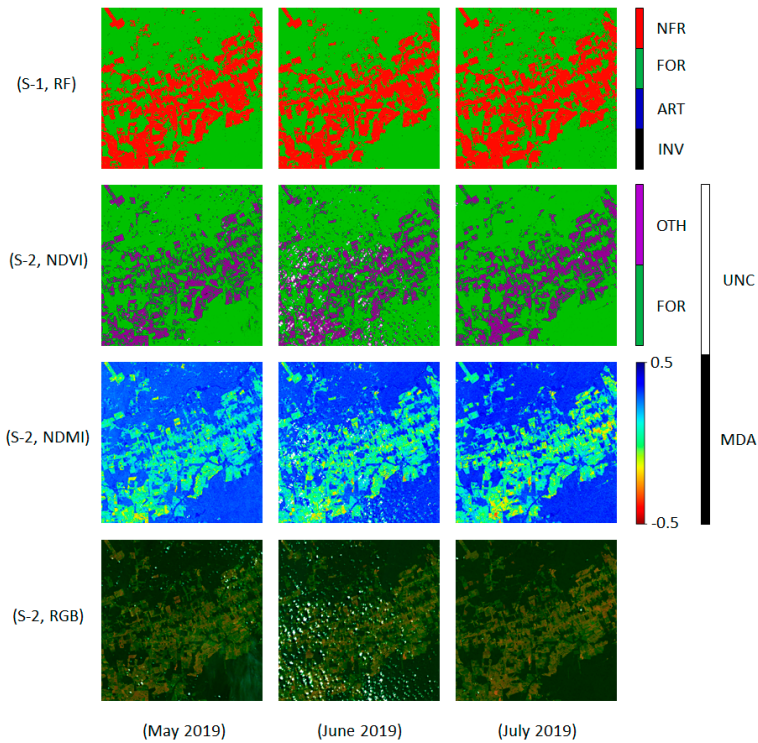


Figure 12. Patch (b): monthly classification comparison between S-1 forest map and S-2 parameters. The same quantities as in Figure 11 are displayed.

S-2 acquisition of May 2019 directly with the one of July 2019, our results identify an additional deforestation area located at the bottom of the image, named (iii) in Figure 11. By observing our S-1 forest map of June 2019, some small-scale activities are visually perceived over the hot spot (iii) before detecting a proper cut later on in July 2019.

Figure 12 depicts a large plantation area on the eastern side of the municipality of Boca do Acre, state of Amazonas. Apart from the S-2 acquisition of June 2019, where many pixels are covered by clouds and their shadows (with a cloud cover percentage of 1.1%), we can observe general stationarity of the scene. However, by jumping from May 2019 to July 2019, we can see some small clearing areas in the upper-right side of the image and also on its left-hand side. These areas are correctly detected by our S-1 forest map if compared with the RGB and NDMI from S-2. In this case, the NDMI index highlights the new cuts as dry pixels, i.e., areas with low water content, not visible within the NDVI image.

Figure 13 presents the southern side of the municipality of Boca do Acre. In this patch we can undoubtedly identify a clear-cut on the upper side of the image, marked with a yellow circle; in this hot spot area, deforestation is moving north, towards Boca do Acre. As mentioned in Section 3, we observe that we may not find S-2 cloud-free acquisitions even during the dry season over the Amazon rainforest. In particular, in June 2019, the cloud cover percentage estimated from the *Unclassified mask* exceeds the 1% for patches (b) and (c). Furthermore, we can see a strong variation of the mostly cloudless acquisition dates for each patch and in each of the three considered months. We utilized the NDVI as a reference mask for evaluating the classification performance of patches (a), (b), and (c) since it represents the best available independent data. Since this mask is binary, we aggregated the classes *non-forested areas* (NFR) and *artificial surfaces* (ART) in the S-1 forest maps. We measured the overall accuracy (OA) and, for the forest class (FOR), also the precision (P), recall (R), and F1-score (F1), which

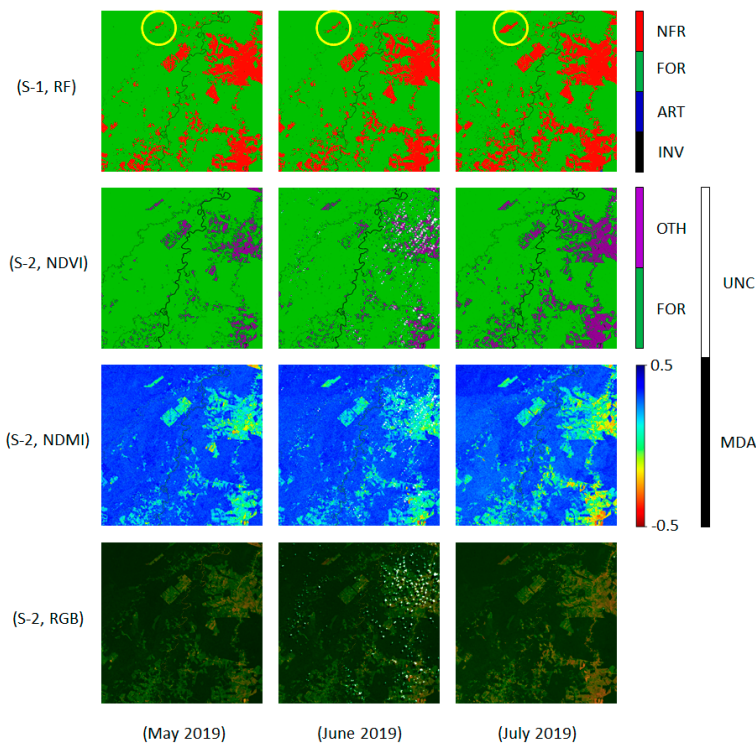


Figure 13. Patch (c): monthly classification comparison between S-1 forest map and S-2 parameters. The same quantities as in Figure 11 are displayed. A hot spot area is marked with yellow circles.

Table 5. Overall accuracy (OA), and, for the FOR class, the precision (P), recall (R), F1-score (F1) of patches (a), (b), and (c). In table we report the date of the S-2 acquisition chosen as reference for the monthly performance evaluation.

	May 2019	June 2019	July 2019
Date	2019.05.09	2019.06.18	2019.07.08
OA	96.11 %	94.78 %	93.89 %
P	98.82 %	98.70 %	99.30 %
R	97.13 %	95.75 %	94.23 %
F1	97.97 %	97.20 %	96.70 %
Date	2019.04.27	2019.06.06	2019.07.01
OA	83.11 %	81.38 %	84.05 %
P	96.70 %	93.85 %	97.74 %
R	80.85 %	80.84 %	80.53 %
F1	88.07 %	86.86 %	88.30 %
Date	2019.05.17	2019.06.11	2019.07.11
OA	87.22 %	86.94 %	89.78 %
P	98.42 %	98.16 %	97.67 %
R	87.43 %	87.58 %	89.98 %
F1	92.60 %	92.57 %	93.66 %

are summarized in Table 5. We can see an overall accuracy of the S-1 forest maps that always exceeds the 80%. As expected, the accuracy values measured for the patch (b) are at least 4% lower than the ones computed for the other patches. We ascribe this behavior to the low reliability of the NDVI mask. Furthermore, we can observe that our classifier can detect the forest class (FOR) with precision always greater than 93% and recall not lower than 80%. Again, for the patch (b), we have lower recall with respect to the one computed for the patch (a) and (c). The F1-Score also shows a similar result, and it always exceeds the 86%.

The final results of our work are depicted in the last row of Figure 14, Figure 15, and Figure 16, which show the evolution in time of deforestation activities in patch (a), patch (b), and patch (c), respectively. All figures are organized into two main bodies. The former comprises a first row that depicts the references, i.e., the FROM-GLC 2017 and the two deforestation masks provided by PRODES in 2018 and 2019. The latter corresponds to the two

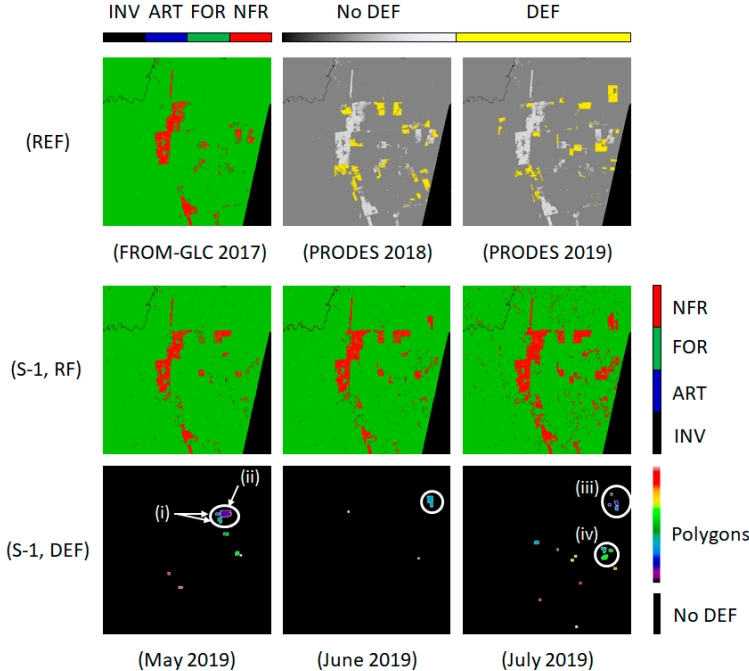


Figure 14. Patch (a): monthly deforestation using S-1 short-time-series. The first row shows the used references: FROM-GLC 2017 and PRODES deforestation (yellow) of 2018 and 2019, both superimposed to the grayscale representation of the FROM-GLC map. The second row depicts the S-1 forest maps of May, June, and July 2019, while the last row shows the results of the watershed segmentation applied after the monthly difference. The clusters of polygons on which deforestation is detected are marked in Roman numerals and with white circles.

last rows and is dedicated to the results: the upper row shows the S-1 forest maps retrieved on the consecutive months of May, June, and July 2019, while the last row refers to the three deforestation maps obtained by applying the processing chain of Figure 5 to the four consecutive forest maps: (1) the modified FROM-GLC map depicted in the first body and the above-mentioned forest maps of (2) May, (3) June and (4) July 2019. In particular, the deforestation map of May 2019 is the difference between the forest map of the current month and the FROM-GLC. The deforestation map of June 2019 refers to the comparison between the forest map of June 2019 and the one of May 2019, and so on. Each deforestation map shows the polygons extracted by applying the watershed segmentation algorithm on the related difference image.

Figure 14 shows the polygons retrieved every month by applying the chain presented in Figure 5 on patch (a). According to the results shown in Figure 11, we can draw the following considerations:

- By analyzing patch (a) in May 2019, we can identify a set of polygons, colored from purple to cyan, and highlighted with a white circle, the changes between the FROM-GLC 2017 and the S-1 forest map generated on that month. The segmentation allows for dividing this cluster of polygons in clear-cuts marked by PRODES in 2018 and 2019. In particular, the cyan polygons, indicated as (i), appear related to activities in 2018, while the bigger one, depicted in purple and marked as (ii), is associated with deforestation recorded in 2019. The purple polygon is a clear-cut created after the 1st of August 2018 but before the end of May 2019. Therefore, our algorithm can increase deforestation maps' temporal resolution by reducing the observation period from one year (as guaranteed by PRODES) to one month.
- Some areas in the lower-left side of the image are classified in PRODES 2018 as clear-cuts, while our algorithm recognizes some of them only in July 2019. The S-2 images of vegetation parameters in Figure 11 confirm the consistency

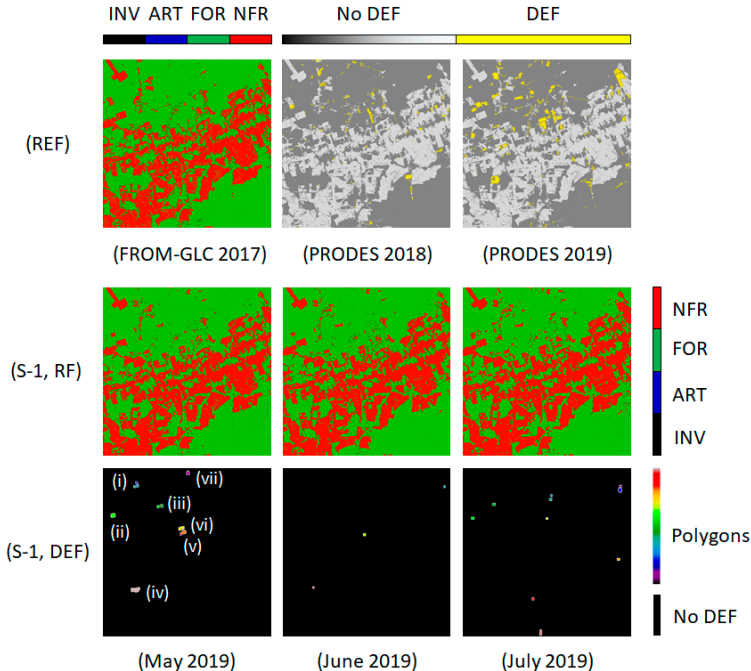


Figure 15. Patch (b): monthly deforestation using S-1 short-time-series. The different quantities are organized as described in Figure 14. The clusters of polygons on which deforestation is detected are marked in Roman numerals.

of our results, and they lead us to assume problems in the reliability of the PRODES maps.

- On the upper-right corner of the image, we can undoubtedly observe the evolution of a clear-cut, firstly detected (cyan polygon, delimited by a white circle) in June 2019, then expanded towards the east (cyan to purple polygons, inside the white circle named (iii)) during July 2019. According to the references, this cut is registered on the PRODES 2019 map only.
- On the right-hand side of the image, we can identify a deforestation activity (green polygons, inside the white circle (iv)) starting after June 2019 and correctly detected in PRODES 2019.

Figure 15 reports the results of the monthly deforestation over patch (b). As expected, more changes are detected during May 2019, since we can count 7 clusters of polygons. By comparing the results of May 2019 with the two deforestation maps of PRODES, we can observe that: those polygons in blue (i), light green (ii), dark green (iii) are marked by PRODES analysts in the year 2018, while the remaining four clusters (white (iv), orange (v),

yellow (vi) and purple (vii)) are identified in 2019. From May to July 2019, small-scale deforestation activities are detected. This result can also be explained by the fact that the area under test is mostly dominated by plantations, as shown in the S-2 RGB maps of Figure 12.

Finally, Figure 16 presents the results of the monthly deforestation over patch (c). According to PRODES maps, this area is not particularly involved in deforestation activities. We can observe two main aspects:

- On the upper side of the image, clear-cuts were detected by PRODES in 2019. Our result suggests that the activity over this area is strongly concentrated in July 2019, marked by our segmentation algorithm as cyan polygons, indicated as (ii). However, our algorithm detects a little polygon in pink (i) in May 2019, which is confirmed by the fine line observed in the S-1 forest map and by the S-2 parameters of Figure 13.
- PRODES deforestation maps of 2018 and 2019 identify an area of deforestation activities in the middle of the image, which is not recognized by

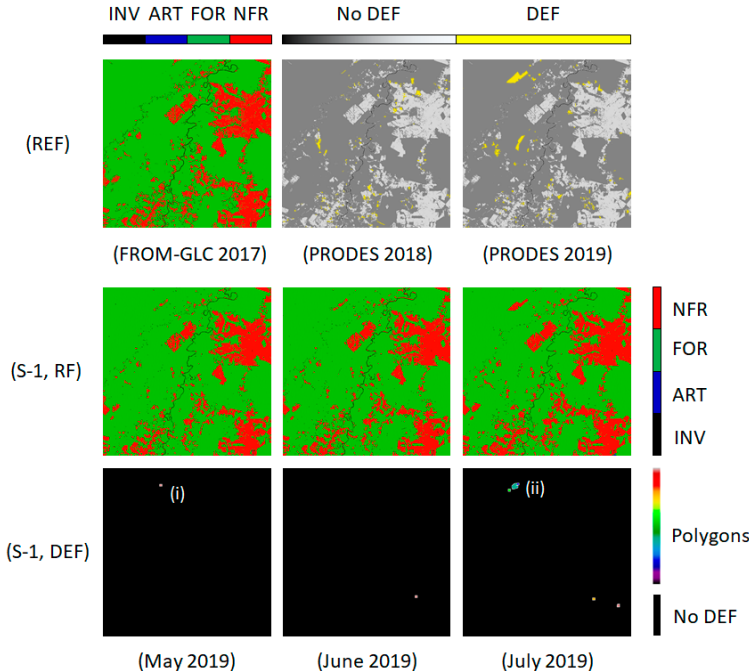


Figure 16. Patch (c): monthly deforestation using S-1 short-time-series. The different quantities are organized as described in Figure 14.

the S-1 forest maps. By observing Figure 13, we can assume that this is a problem of sensor sensitivity since neither the S-2 NDVI index nor the S-2 NDMI one recognizes this hotspot. However, it is worth highlighting that the S-2 RGB map also shows a thin line on this area whose shape can recall the clear-cut detected by PRODES 2019.

5. Conclusions

The experiments reported in this paper confirm the high potential of multi-temporal interferometric short-time-series for forest mapping and deforestation monitoring. Indeed, by systematically iterating the proposed processing chain, we tested a simple change detection algorithm based on subsequent multi-temporal stacks and watershed segmentation. In the experimental results, we showed that short-time-series could be successfully exploited to timely detect deforestation processes. In particular, we can follow deforestation trends monthly, without any influence of cloud cover. This aspect is crucial for developing an effective early-warning system, able to detect changes in the Amazon basin automatically.

The results highlighted possible sources of uncertainties coming from the three reference maps considered in this analysis:

- The FROM-GLC map is older than the exploited S-1 time-series, causing a mismatch due to temporal changes. Furthermore, as we already pointed out in Pulella et al. (2020), this map is more sensitive to sparse vegetation with respect to S-1, minimizing bare soil and rocky surface areas.
- The PRODES map has a lower temporal and spatial resolution. Indeed, it is provided on a yearly base by mapping the new clear-cuts. Furthermore, it has a coarser actual resolution due to a minimum-mapping-area of 6.25 hectares, and it is hand-marked by analysts and may present imprecision due to human errors.
- The S-2 NDVI map is impaired from cloud coverage, which is very common in areas like the Amazon rainforest. Therefore, it cannot always provide a temporal and spatial continuity of the data. Furthermore, the SCL product, which provides a cloud (and cloud shadow) map, can present errors, which are a further mismatch source.

Future investigation will regard the development of new strategies for pre-serving data resolution. On the one hand, we can improve the estimation of the interferometric parameters using advanced processing techniques that exploit InSAR signal statistic on the single interferometric pair with nonlocal patch-based approaches (Sica et al., 2018), deep learning methods (Sica et al., 2020), or the whole temporal stacks (Sica et al., 2015). On the other hand, we can directly act on the classification procedure by exploiting deep learning semantic segmentation and using the estimated coherence together or in place of customized features (Lyu et al., 2016).

Acknowledgments

The performed work has been partially financed through the HI-FIVE project, granted by the ESA Living Planet Fellowship 2018. The authors gratefully acknowledge the Sentinel-1 mission management, in the person of Luca Martino and Pierre Potin, for providing an additional acquisition scheduling over the state of Rondonia.

References

- Belgiu, M., Drăguț, L. 2016. Random forest in remote sensing: A review of applications and future directions. *ISPRS journal of photogrammetry and remote sensing*, 114, 24-31. <https://doi.org/10.1016/j.isprsjprs.2016.01.011>
- Beucher, S., Meyer, F. 1993. The morphological approach to segmentation: the watershed transformation. *Mathematical morphology in image processing*, 34, 433-481. <https://doi.org/10.1201/9781482277234-12>
- Bontemps, S., Defourny, P., Bogaert, E. V., Arino, O., Kalogirou, V., Perez, J. R. 2011. *GLOBCOVER 2009 Product description and validation report. tech. rep.*, European Space Agency, Feb. 2011.
- Breiman, L. 2001. Random Forests. *Machine Learning*, 45, 5-32. <https://doi.org/10.1023/A:1010933404324>
- Bueso-Bello, J.L., Rizzoli, P., Martone, M., Gonzalez, C. 2018. Potentials of TanDEM-X Forest/Non-forest Map for Change Detection. In *International Geoscience and Remote Sensing Symposium (IGARSS)*, pp. 4213-4216. <https://doi.org/10.1109/IGARSS.2018.8517867>
- Diniz, F.H., Kok, K., Hott, M.C., Hoogstra-Klein, M.A., Arts, B. 2013. From space and from the ground: determining forest dynamics in settlement projects in the Brazilian Amazon. *International Forestry Review*, 15(4), 442-455. <https://doi.org/10.1505/146554813809025658>
- Dobson, M.C., Ulaby, F.T., Pierce, L.E. 1995. Land-cover classification and estimation of terrain attributes using synthetic aperture radar. *Remote sensing of Environment*, 51(1), 199-214. [https://doi.org/10.1016/0034-4257\(94\)00075-X](https://doi.org/10.1016/0034-4257(94)00075-X)
- Drusch, M., Del Bello, U., Carlier, S., Colin, O., Fernandez, V., Gascon, F., Hoersch, B., Isola, C., Labertini, P., Martimort, P., Meygret, A., Spoto, F., Sy, O., Marchese, F., Bargellini, P. 2012. Sentinel-2: ESA's optical high-resolution mission for GMES operational services. *Remote sensing of Environment*, 120, 25-36. <https://doi.org/10.1016/j.rse.2011.11.026>
- Dubayah, R.O., Drake, R.O., 2000. Lidar remote sensing for forestry. *Journal of Forestry*, 98, 44-46.
- Ellatifi, M. 2009. Forests in the Biosphere, in J.N. Owens and H.G. Lund, (eds.) *Forests And Forest Plants - Volume III*, ch. 1, pp. 1–20, Oxford, UK: EOLSS Publishers Co. Ltd.
- Friedl, M.A., Sulla-Menashe, D., Tan, B., Schneider, A., Ramankutty, N., Sibley, A., Huang, X. 2010. MODIS Collection 5 global land cover: Algorithm refinements and characterization of new datasets. *Remote sensing of Environment*, 114(1), 168-182. <https://doi.org/10.1016/j.rse.2009.08.016>
- Gong, P., Liu, H., Zhang, M., Li, C., Wang, J., Huang, H., Clinton, N., Ji, L., Li, W., Bai, Y., Chen, B., Xu, B., Zhu, Z., Yuan, C., Suen, H.P., Guo, J., Xu, N., Li, W., Zhao, Y., Yang, J., Yu, C., Wang, X., Fu, H., Yu, L., Dronova, I., Hui, F., Cheng, X., Shi, X., Xiao, F., Liu, Q., Song, L. 2019. Stable classification with limited sample: Transferring a 30-m resolution sample set collected in 2015 to mapping 10-m resolution global land cover in 2017. *Sci Bull*, 64(6), 370-373. <https://doi.org/10.1016/j.scib.2019.03.002>
- Hansen, M. C., Potapov, P. V., Moore, R., Hancher, M., Turubanova, S. A., Tyukavina, A., Tau, D., Stehman, S.V., Goetz, S.J., Loveland, T.R., Kommareddy, A., Egorov, A., Chini, L., Justice, C.O., Townshend, J.R.C. 2013. High-resolution global maps of 21st-century forest cover change. *Science*, 342(6160), 850-853. <https://doi.org/10.1126/science.1244693>
- Kalamandeen, M., Gloor, E., Mitchard, E., Quincey, D., Ziv, G., Spracklen, D., Spracklen, B., Adami, M., Aragão, L., Galbraith, D. 2018. Pervasive rise of small-scale deforestation in Amazonia. *Scientific reports*, 8(1), 1-10. <https://doi.org/10.1038/s41598-018-19358-2>
- Lu, X., Yuan, Y., Zheng, X. 2017. Joint dictionary learning for multispectral change detection. *IEEE transactions on cybernetics*, 47(4), 884-897. <https://doi.org/10.1109/TCYB.2016.2531179>

- Lyu, H., Lu, H., Mou, L. 2016. Learning a transferable change rule from a recurrent neural network for land cover change detection. *Remote Sensing*, 8(6), 506. <https://doi.org/10.3390/rs8060506>
- Main-Knorn, M., Pflug, B., Louis, J., Debaecker, V., Müller-Wilm, U., Gascon, F. 2017. Sen2Cor for Sentinel-2. In *Image and Signal Processing for Remote Sensing XXIII*, vol. 10427, pp. 37-48. International Society for Optics and Photonics, SPIE. <https://doi.org/10.1117/12.2278218>
- Malenovský, Z., Rott, H., Cihlar, J., Schaepman, M.E., García-Santos, G., Fernandes, R., Berger, M. 2012. Sentinels for science: Potential of Sentinel-1,-2, and-3 missions for scientific observations of ocean, cryosphere, and land. *Remote Sensing of environment*, 120, 91-101. <https://doi.org/10.1016/j.rse.2011.09.026>
- Malhi, Y., Roberts, J.T., Betts, R.A., Killeen, T.J., Li, W., Nobre, C.A. 2008. Climate Change, Deforestation, and the Fate of the Amazon. *Science*, 319(5860), 169-172.
- Martone, M., Rizzoli, P., Wecklich, C., González, C., Bueso-Bello, J.L., Valdo, P., Schulze, D., Zink, M., Krieger, G., Moreira, A. 2018. The global forest/non-forest map from TanDEM-X interferometric SAR data. *Remote sensing of environment*, 205, 352-373. <https://doi.org/10.1016/j.rse.2017.12.002>
- Martone, M., Sica, F., González, C., Bueso-Bello, J.L., Valdo, P., Rizzoli, P. 2018. High-resolution forest mapping from tandem-x interferometric data exploiting nonlocal filtering. *Remote Sensing*, 10(9), 1477. <https://doi.org/10.3390/rs10091477>
- Mazza, A., Sica, F., Rizzoli, P., Scarpa, G. 2019. TanDEM-X Forest Mapping Using Convolutional Neural Networks. *Remote Sensing*, 11(24), 2980. <https://doi.org/10.3390/rs11242980>
- Montibeller, B., Kmoch, A., Virro, H., Mander, Ü., Uuemaa, E. 2020. Increasing fragmentation of forest cover in Brazil's Legal Amazon from 2001 to 2017. *Scientific reports*, 10(1), 1-13. <https://doi.org/10.1038/s41598-020-62591-x>
- Mora, B., Tsendbazar, N.E., Herold, M., Arino, O. 2014. Global land cover mapping: Current status and future trends. In *Land Use and Land Cover Mapping in Europe* (pp. 11-30). Springer, Dordrecht. https://doi.org/10.1007/978-94-007-7969-3_2
- Perigolo, N.A., de Medeiros, M.B., Simon, M.F. 2017. Vegetation types of the upper Madeira River in Rondônia, Brazil. *Brittonia*, 69(4), 423-446. <https://doi.org/10.1007/s12228-017-9505-1>
- Pulella, A., Aragão Santos, R., Sica, F., Posovszky, P., Rizzoli, P. 2020. Multi-temporal sentinel-1 backscatter and coherence for rainforest mapping. *Remote Sensing*, 12(5), 847. <https://doi.org/10.3390/rs12050847>
- Shimada, M., Itoh, T., Motooka, T., Watanabe, M., Shiraishi, T., Thapa, R., Lucas, R. 2014. New global forest/non-forest maps from ALOS PALSAR data (2007–2010). *Remote Sensing of environment*, 155, 13-31. <https://doi.org/10.1016/j.rse.2014.04.014>
- Shvidenko, A.Z., Schepaschenko, D.G. 2013. Climate change and wildfires in Russia. *Contemporary Problems of Ecology*, 6, 683-692.
- Sica, F., Reale, D., Poggi, G., Verdoliva, L., Fornaro, G. 2015. Nonlocal adaptive multilooking in SAR multipass differential interferometry. *IEEE Journal of Selected Topics in Applied Earth Observations and Remote Sensing*, 8(4), 1727-1742. <https://doi.org/10.1109/JSTARS.2015.2421554>
- Sica, F., Cozzolino, D., Verdoliva, L., Poggi, G. 2018. The offset-compensated nonlocal filtering of interferometric phase. *Remote Sensing*, 10(9), 1359. <https://doi.org/10.3390/rs10091359>
- Sica, F., Pulella, A., Nannini, M., Pinheiro, M., Rizzoli, P. 2019. Repeat-pass SAR interferometry for land cover classification: A methodology using Sentinel-1 Short-Time-Series. *Remote Sensing of Environment*, 232, 111277. <https://doi.org/10.1016/j.rse.2019.111277>
- Sica, F., Bretzke, S., Pulella, A., Bueso-Bello, J.L., Martone, M., Prats-Iraola, P., González-Bonilla, M.J., Schimtt, M., Rizzoli, P. 2020. InSAR Decorrelation at X-Band From the Joint TanDEM-X/PAZ Constellation. *IEEE Geoscience and Remote Sensing Letters*. <https://doi.org/10.1109/LGRS.2020.3014809>
- Sica, F., Gobbi, G., Rizzoli, P., Bruzzone, L. 2020. φ-Net: Deep Residual Learning for InSAR Parameters Estimation. *IEEE Transactions on Geoscience and Remote Sensing*. pp. 1-25. <https://doi.org/10.1109/TGRS.2020.3020427>
- Stone, T.A., Brown, I.F., Woodwell, G.M. 1991. Estimation, by remote sensing, of deforestation in central Rondônia, Brazil. *Forest Ecology and Management*, 38(3-4), 291-304. [https://doi.org/10.1016/0378-1127\(91\)90150-T](https://doi.org/10.1016/0378-1127(91)90150-T)
- Torres, R., Snoeij, P., Geudtner, D., Bibby, D., Davidson, M., Attema, E., Potin, P., Rommen, B., Flouri, N., Brown, M., Traver, I.N., Deghaye, P., Duesmann, B., Rosich, B., Miranda, N., Bruno, C., L'Abbate, M., Croci, R., Pietrapaolo, A., Huchler, M., Rostan, F. 2012. GMES Sentinel-1 mission. *Remote Sensing of Environment*, 120, 9-24. <https://doi.org/10.1016/j.rse.2011.05.028>

Unser, M. 1986. Sum and Difference Histograms for Texture Classification. *IEEE Transactions on Pattern Analysis and Machine Intelligence*, PAMI-8, 1, 118-125. <https://doi.org/10.1109/TPAMI.1986.4767760>

Valeriano, D.M., Mello, E.M., Moreira, J.C., Shimabukuro, Y.E., Duarte, V., Souza, I.M., do Santos, J.R., Barbosa, C.C.F., de Souza, R.C.M. 2004. Monitoring tropical forest from space: the PRODES digital project. *International Archives of Photogrammetry Remote Sensing and Spatial Information Sciences*, 35, 272-274.

Wen, D., Huang, X., Zhang, L., Benediktsson, J.A. 2016. A novel automatic change detection method for urban high-resolution remotely sensed imagery based on multiindex scene representation. *IEEE Transactions on Geoscience and Remote Sensing*, 54(1), 609-625. <https://doi.org/10.1109/TGRS.2015.2463075>

Wilson, E.H., Sader, S.A. 2002. Detection of forest harvest type using multiple dates of Landsat TM imagery. *Remote Sensing of Environment*, 80(3), 385-396. [https://doi.org/10.1016/S0034-4257\(01\)00318-2](https://doi.org/10.1016/S0034-4257(01)00318-2)